Simultaneous and real-time measurement of slope and curvature fringes in thin structures using shearing interferometery

Hareesh V. Tippur
Auburn University
Department of Mechanical Engineering
Auburn, Alabama 36849
E-mail: htippur@eng.auburn.edu

Abstract. A real-time lateral shearing interferometry that uses a pair of Ronchi gratings to perform wavefront shearing operations is described for measuring slope and curvature fringes simultaneously in thin structures. It involves simultaneous imaging of diffracted wavefronts using Fourier filtering. Two sets of fringe patterns, one representing slopes and the other curvatures, occur simultaneously at spatially distinct locations on the image plane, thereby eliminating the need for additional postprocessing of the recordings. In this work, the principles involved in the measurement of slopes and curvatures using this technique are explained. The method is then demonstrated on thin structures subjected to well-defined loading conditions, such as a clamped circular silicon wafer subjected to central displacement. Measurements have been successfully compared with analytical solutions. © *2004 Society of Photo-Optical Instrumentation Engineers.* [DOI: 10.1117/1.1809611]

Subject terms: shearing interferometry; Ronchi gratings; thin structures; slope; curvature.

1 Introduction

Tremendous progress in microelectronics and microelectro-mechanical systems (MEMS) has occurred in recent years. These systems generally consist of thin structures involving layered dissimilar materials or thin-film coatings on substrates. Process and service-induced stresses due to mismatch in thermomechanical material properties are common in these configurations, and accurate quantification of the same is needed for characterizing processes as well as resulting component reliability.[1] It is well known that stresses in thin plate-like structures can be evaluated by knowing surface slopes and curvatures. This observation has been widely utilized by a number of investigators in the past to measure surface slopes and curvatures *separately* using both coherent and incoherent optical metrology. These methods can be broadly classified into 1. real-time methods[2–6] and double-exposure schemes[7,8] involving specularly reflective objects, and 2. double-exposure schemes for diffusely reflective surfaces.[9,10]

Among the real-time slope and curvature measurement methods for specular objects, Assa, Betser, and Politch[3] have demonstrated different grating shearing interferometers. Using diffraction analysis, they have shown that one of their arrangements can give slope fringes in real time, but a second, however, needs spatial filtering to obtain the same. Their setup is capable of providing curvatures but needs spatial filtering of the recordings. In their review article, Kao and Chiang[3] have described a family of optical arrangements that incorporate single and double line gratings to accurately measure slopes and curvatures using both single- and double-exposure schemes. They have used geometric moiré principles to develop the governing equations as they use relatively coarse gratings. A modified reflection moiré method proposed by Ritter and Schettler-Koehler[4] is capable of providing curvature fringes in real time. Selective diffraction order filtering is utilized by Subramanian et al.[5,6] to obtain slopes and curvatures sequentially in real time. Subsequent optical spatial filtering is needed in some arrangements to acquire the necessary information.

It is evident that although some of these methods can provide slopes and curvatures in real time, postprocessing of the recordings is often needed to retrieve both slopes and curvatures, since the information is not available on the image plane at spatially distinct locations. The current work demonstrates the feasibility of a double-grating lateral shearing interferometer called coherent gradient sensing (CGS), used widely in failure mechanics[11] studies, and more recently for thin film characterization,[12] for simultaneously measuring surface slope and curvature fringes from specularly reflective thin structures in real time. Previously, it had not been realized that the optical arrangement, which had been used for slope measurements only, can be easily adopted for extracting curvatures as well as slopes. It requires no postprocessing of image plane recordings, since the two families of fringes occur at spatially distinct locations. This capability could be valuable for characterizing transient processes such as metallic thin-film deposition and polymeric coating and curing.

2 Experimental Setup

The experimental setup used is shown schematically in Fig. 1. It consists of a polished silicon wafer (diameter 50.8 mm, 500 μm thick) bonded to a steel disk with a central aperture of diameter 25.4 mm. The wafer is illuminated by
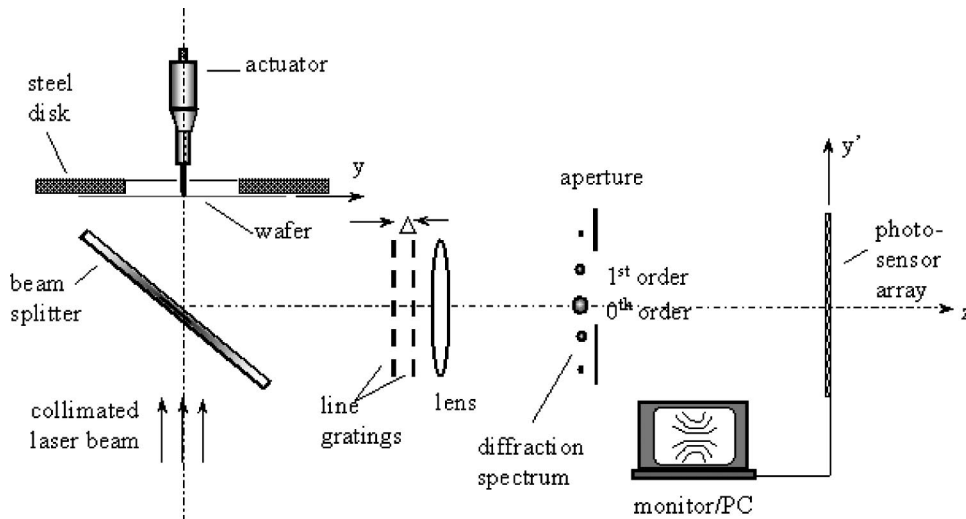
Fig. 1 Schematic of the experimental setup for reflection coherent gradient sensing (CGS).

a collimated He-Ne laser beam. The reflected object wavefront is transmitted through two parallel Ronchi gratings (25.4-μm pitch) separated by a distance (Δ) of 24 mm. The diffracted wavefronts are collected by a plano-convex lens (focal length 500 mm), and the resulting diffraction spectrum is registered on its focal plane as shown. An aperture is used to block all but the necessary diffraction orders as depicted. The interferograms are recorded by a charge-coupled device (CCD) array located at the image plane in real time. It should be emphasized that the camera system comprised of the lens and the photosensor array is focused on the object surface using a target placed at the wafer plane during optical alignment. That is, the object and image distances obey the lens law.

The gratings used in this study are chrome-on-glass line-pair depositions with magnesium fluoride antireflection coating. The choice of master Ronchi grating plates is dictated by the commercial availability, and the method should function equally well with other grating profiles such as sinusoidal rulings. It should also be noted that antireflection coatings are essential for minimizing image noise in the form of ghost fringes, which would otherwise occur due to multiple reflections between the gratings. Other parameters such as grating pitch, grating separation distance, and focal length of the imaging lens are chosen based on the need for 1. producing sufficient spatial shearing of the object wavefront without unduly compromising the accuracy of derivative representation of the out-of-plane displacements, 2. separating the diffraction spots at the back focal plane of the imaging lens sufficiently for easy filtering, and 3. separating slope and curvature fringes spatially on the image plane to avoid additional postprocessing. The use of commercially available micropositioning devices to control in-plane and out-of-plane parallelism between gratings and grating lines limit the grating separating distance to be no less than 15 mm in the current setup.

3 Optical Analysis

The object wave, making an angle ϕ with the optical axis in the y-z plane, is transmitted through a pair of Ronchi grat-

ings G_1 and G_2 of pitch p with principal grating direction, say, along y axis (Fig. 2). The separation distance between the two gratings along the optical axis is Δ. The resulting diffracted light emerging from the first grating consists of a zero and several odd diffraction orders, each denoted by the corresponding complex amplitude distribution E. For simplicity, only consider diffraction orders $E_i(i=0,\pm1)$ after the first grating. These waves are propagating in discretely different directions according to the diffraction equation $[\theta=\sin^{-1}(\lambda/p)\approx(\lambda/p)$ for small angles]. Each of these diffracted wavefronts diffract again at the second grating plane, and the corresponding wavefronts propagating in several discrete directions are denoted by $E_{(i,j)}$ ($i=0,\pm1,j=0,\pm1$), where the subscripts correspond to diffraction order at the first and second grating, respectively. The wavefronts $E_{\pm1,0}$ and $E_{0,\pm1}$ contribute to the ±1 diffraction spot on the focal plane. And, diffracted wavefronts $E_{0,0}$, $E_{+1,-1}$, and $E_{-1,+1}$ contribute to the zero order. By letting ±1 or 0 diffraction order pass through the filtering aperture, interference fringes resulting from the corresponding complex amplitudes can be evaluated. Let l_0 and $l_{\pm1}$ denote the optical path lengths of E_0 and $E_{\pm1}$, respectively, between the two gratings. Then, complex amplitudes E_0 and $E_{\pm1}$ can be represented as $E_0=C_0\exp(ikl_0)$, $E_{\pm1}=C_{\pm1}\exp(ikl_{\pm1})$, where Cs denotes amplitudes, k denotes the wave number ($=2\pi/\lambda$), and $i=\sqrt{-1}$. Noting that no additional path difference occurs beyond the grating G_2, the intensity distribution on the CCD array for a 1:1 magnification is proportional to,

$$
\begin{aligned}
I_{\pm1} &= (E_{0,\pm1}+E_{\pm1,0})(E_{0,\pm1}+E_{\pm1,0})^* \\
&= A_0^2+A_{\pm1}^2+2A_0A_{\pm1}\cos k(l_0-l_{\pm1}),
\end{aligned}
\tag{1}
$$

when ±1 diffraction spot is let through the aperture and,

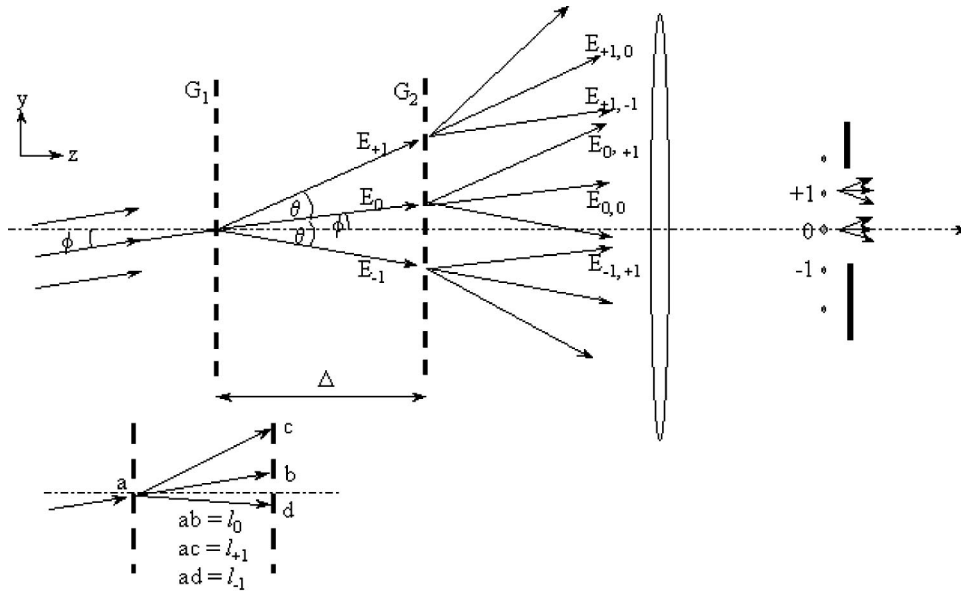**Fig. 2** Schematic representation of diffraction and Fourier filtering of wavefronts in CGS.

$$I_0 = (E_{0,0} + E_{+1,0} + E_{0,-1})(E_{0,0} + E_{+1,0} + E_{0,-1})^*$$
$$= A_0^2 + A_{+1}^2 + A_{-1}^2 + 2A_0A_{+1}\cos k(l_0 - l_{+1})$$
$$+ 2A_0A_{-1}\cos k(l_0 - l_{-1})$$
$$+ 2A_{+1}A_{-1}\cos k(l_{+1} - l_{-1}), \tag{2}$$

when a zero-order diffraction spot is let through the aperture at the spectrum plane. In the previous, I_0 and $I_{\pm 1}$ denote the intensity, A_0 and $A_{\pm 1}$ the constant amplitudes associated with each diffracted wavefront after grating G_2, and $*$ denotes the complex conjugate. Based on geometrical considerations, the optical path lengths l_0 and $l_{\pm 1}$ can be expressed as,

$$l_0 = \frac{\Delta}{\cos\phi} = \frac{\Delta}{\left(1 - \frac{\phi^2}{2!} + \frac{\phi^4}{4!} - \cdots\right)},$$

$$l_{\pm 1} = \frac{\Delta}{\cos(\theta \pm \phi)} = \frac{\Delta}{\left[1 - \frac{(\theta \pm \phi)^2}{2!} + \frac{(\theta \pm \phi)^4}{4!} - \cdots\right]}, \tag{3}$$

by expanding $\cos(\cdot)$ in the neighborhood of $(\cdot) = $ zero. For *small angles*, when the series is truncated by neglecting the terms of the order of $(\cdot)^3$ and beyond, Eq. (3) becomes,

$$l_0 \approx \frac{\Delta}{\left(1 - \frac{\phi^2}{2!}\right)} \approx \Delta\left(1 + \frac{\phi^2}{2}\right),$$

$$l_{\pm 1} \approx \frac{\Delta}{\left[1 - \frac{(\theta \pm \phi)^2}{2!}\right]} \approx \Delta\left[1 + \frac{(\theta \pm \phi)^2}{2}\right], \tag{4}$$

where binominal expansion

$$(1 \pm p)^q = \left[1 \pm \frac{q}{1!}p + \frac{q(q-1)}{2!}p^2 \pm \frac{q(q-1)(q-2)}{3!}p^3 + \cdots\right]$$

for $(p^2 < 1, q \neq 0,1,2,...)$ is used.

3.1 Filtering Out All but ± 1 Diffraction Order

By calculating the path difference $(l_0 - l_{\pm 1})$ from Eq. (4), the expression for intensity distribution Eq. (1) on the sensor/image plane when the $\pm$ first diffraction order is allowed to pass through the filtering aperture is,

$$I_{\pm 1} \approx A_0^2 + A_{\pm 1}^2 + 2A_0A_{\pm 1}\cos\left[k\Delta\left(\frac{\theta^2}{2} \pm \theta\phi\right)\right]. \tag{5}$$

Then, constructive interference occurs when the argument of the cosine term in the prior equation is $2N_d\pi$, where $N_d = 0, \pm 1, \pm 2,...$, is the fringe order. After substituting for the wave number, we get

$$\frac{\Delta}{\lambda}\theta\left(\frac{\theta}{2} \pm \phi\right) = N_d.$$

When the wafer is undeformed ($\phi = 0$), the fringe order of the uniform bright fringe of the undeformed wafer can be denoted by $N_u = \Delta/p\,(\theta/2) = $ constant $(N_u = 0, \pm 1, \pm 2,...,)$, where $\theta \approx \lambda/p$ is utilized. By incorporating the expression for N_u, the magnitude of angular deflection of light at a point on the wafer surface can be written as,

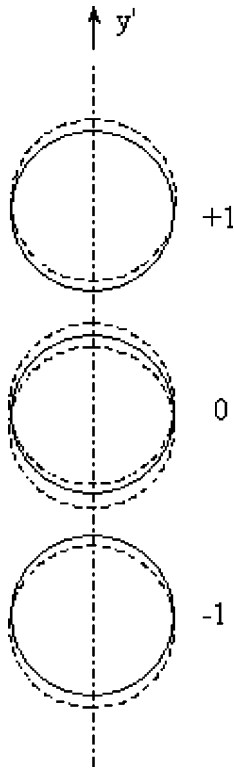$$\phi = (N_d - N_u)\frac{p}{\Delta} = n\frac{p}{\Delta}, \quad n = 0, \pm 1, \pm 2,\ldots. \tag{6}$$

Fig. 3 Overlapping sheared wavefronts on the image plane (x'-y' plane) for filtering all but $+1$, 0, -1 diffraction spots. The solid and broken circles correspond to zero order and $+1$ or -1 diffraction orders passing though the aperture, respectively

Since angular deflection of light rays can be related to surface slopes as $\phi = 2(\partial w/\partial y)$, where w is the out-of-plane deflection of the wafer in the z direction, surface slopes can be quantified as $\partial w/\partial y \approx \delta w/\delta y = n\,p/2\Delta$, where δ is the difference operator. It should be noted that the interference fringes obtained by filtering all but $+1$ or -1 diffractions can be interpreted as forward and backward differences of the optical signal. The fringe formation in the overlapping region can be schematically represented as in Fig. 3, where the solid line is used to represent the undiffracted wave, and the dotted line represents either a $+1$ or -1 wavefront. Evidently, the sensitivity of the interferometer for measuring angular deflections of light (and hence, surface slope) depends on the ratio of grating pitch p and grating separation distance Δ, providing experimental flexibility in choosing p and Δ, clearly an added experimental advantage.

3.2 Filtering Out All but Zero Diffraction Order

After substituting the path differences $(l_0 - l_{\pm 1})$ and $(l_{+1} - l_{-1})$ in Eq. (2), intensity distribution on the image plane becomes,

$$I_0 = (A_0^2 + A_{+1}^2 + A_{-1}^2) + 2A_0A_{+1}\cos k\Delta\left(\frac{\theta^2}{2} + \theta\phi\right)$$

$$+ 2A_0A_{-1}\cos k\Delta\left(\frac{\theta^2}{2} - \theta\phi\right)$$

$$+ 2A_{+1}A_{-1}\cos k\Delta(2\theta\phi). \qquad (7)$$

This corresponds to overlapping 0, $+1$, and -1 diffractions as shown schematically in Fig. 3. Equation (7) comprises three individual intensities represented by the three cosine terms. The arguments of the first and second cosine terms are identical to the one in Eq. (5), and hence, intensity distributions correspond to forward and backward differences, respectively. Further, these two terms are of equal visibility since the coefficients multiplying them are equal ($=2A_0A_{+1}$). The third cosine term represents an intensity distribution pertaining to the parameter 2ϕ. However, visibility of the fringes is substantially low due to the coefficient $2A_{+1}A_{-1}$. Thus, the observed intensity consists of two identical, overlapping, and spatially shifted fringe patterns. This causes a moiré-of-moiré effect[13] and produces a new set of fringes. Since the overlapping fringes denote $(\delta w/\delta y)$, moiré-of-moiré fringes represent,

$$\frac{\delta}{\delta y}\left(\frac{\delta w}{\delta y}\right) = \frac{\delta}{\delta y}\left(n\frac{p}{2\Delta}\right) = \frac{p}{2\Delta}\left(\frac{\delta n}{\delta y}\right) = \frac{pm}{2\Delta(\delta y)},$$

$$m = 0, \pm 1, \pm 2..., \qquad (8)$$

where δy is the shearing distance and m is the order of the curvature fringes. Equation (8) suggests that the sensitivity of the curvature fringes is intimately linked to the density of the slope fringes and the shearing distance.

4 Initial Optical Alignment

The shearing interferometer needs to be aligned initially to ensure 1. planarity of the incident laser beam used for interrogating the surface of the thin structure and 2. parallelism of the Ronchi gratings G_1 and G_2 as well as the grating lines. This is accomplished by mounting gratings G_1 and G_2 on positioning devices. One of the two gratings, say G_2, is mounted on a micropositioning device with z-direction translation and rotational capabilities about the z axis. Separate coarse rotational capabilities about the x and y axes for G_1 are also needed. First, parallelism between the grating planes G_1 and G_2 can be ensured using the coarse positioning device for G_1 by rotating G_1 relative to G_2 about the x and y axes. The collimation of the laser beam can then be ensured by using a front-coated mirror of a relatively high degree of flatness such as a $\lambda/4$ or $\lambda/8$ mirror as the object. Assuming parallelism between grating lines of G_1 and G_2, when the incident beam is a spherical wavefront $i(x,y) = x^2 + y^2/2f$, f being the focal length of the collimating lens, a fringe pattern, as shown in Fig. 4(a), would result on the image plane when the principal direction of the Ronchi gratings is along the y axis. Now, a planar wavefront can be obtained by adjusting the collimator to widen the fringe spacing until a uniform light fringe covers the entire field of view. For a planar wavefront incident on the gratings, the rotational misalignment such as the one shown in Fig. 4(b) would result in equally spaced fringes along the principal direction of the gratings. The formation of these fringes is due to coherent self-imaging phenomenon[14] along the z axis at Talbot intervals $Z_T = 2p^2/\lambda$. These rotational fringes can be eliminated by rotating G_2 about the z axis until the fringe spacing increases and a single light fringe covers the entire field of
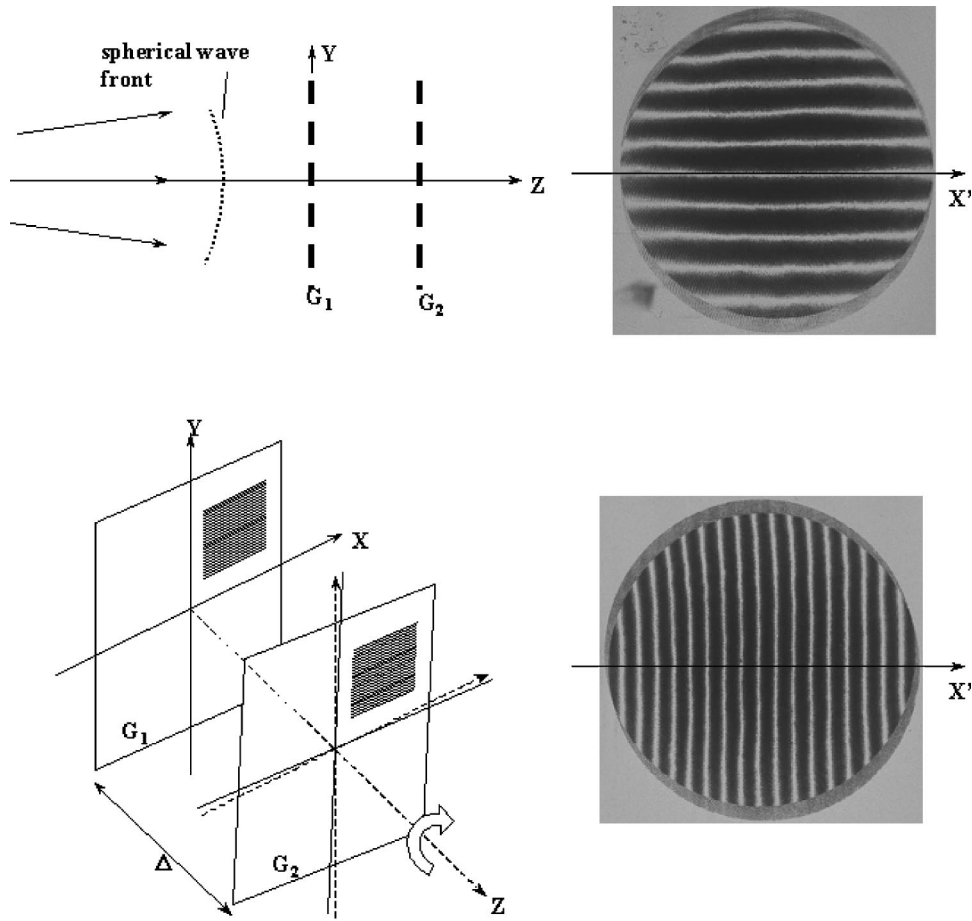
Fig. 4 Optical alignment fringes when the principal direction of the gratings is along the *y* axis. (a) Fringes due to spherical wavefront, and (b) fringes due to relative rotational misalignment between gratings

view. In reality, however, both these misalignments occur together, resulting in equally spaced fringe at an arbitrary angle relative to the principal direction of the gratings. Thus, optical alignment will have to be carried out iteratively until a uniform light fringe covers the entire field of view.

5 Experimental Results

The method is demonstrated by performing benchmark experiments on a clamped circular silicon wafer subjected to a known central displacement. The wafer was bonded to a steel substrate with a 25.4-mm central aperture using a thin layer of epoxy. Interference fringes representing surface slopes and curvatures for an imposed central deflection of 80 μm is shown in Figs. 5(a) and 6(a), respectively. A uniform light field representing zero slope and curvature surrounds the fringes in the plate. Excellent fringe contrast and symmetry are evident from the interferograms. The fringes at the center of the plate are very dense in view of the concentrated force acting at that point. Despite this, the fringes are highly discernible, as shown in the enlarged view of the slope and curvature fringes in Figs. 5(b) and 6(b). The slope fringe [Fig. 5(a)] orders increase monotonically from a zero value along the *x* axis to a maximum value along the *y* axis, beyond which fringe orders reduce

back to zero at the edge of the plate. Fringe contours represent a surface slope of 2.64×10^{-4} radians/half-fringe. The moiré-of-moiré fringes representing curvature [Fig. 6(a)] are numbered according to the principle of moiré fringe formation. That is, when one set of slope fringe overlays exactly on top of the second set, an integer fringe order is assigned. Accordingly, a zero-order fringe is seen along the *x* axis at the edge of the plate. Further, the zero-order fringe passes through the location of maximum slope fringe along the *y* axis. For the chosen experimental parameters, the curvature fringes represent 0.44 m^{-1} per half-fringe.

Quantitative comparison between optical measurements and the thin-plate theory is made next. The surface slopes and curvatures of a centrally loaded clamped plate are given by,

$$
\frac{\partial w}{\partial y} = \frac{4 y w_{\max}}{a^2} \log\left(\frac{\sqrt{x^2 + y^2}}{a} \right),
$$

$$
\frac{\partial^2 w}{\partial y^2} = \frac{4 w_{\max}}{a^2} \log\left(\frac{\sqrt{x^2 + y^2}}{a} \right) + \frac{4 y^2 w_{\max}}{a^2 (x^2 + y^2)},
$$

(9)

where $w_{\max}$ and a denote the maximum out-of-plane displacement and plate radius, respectively, and (x, y) denote
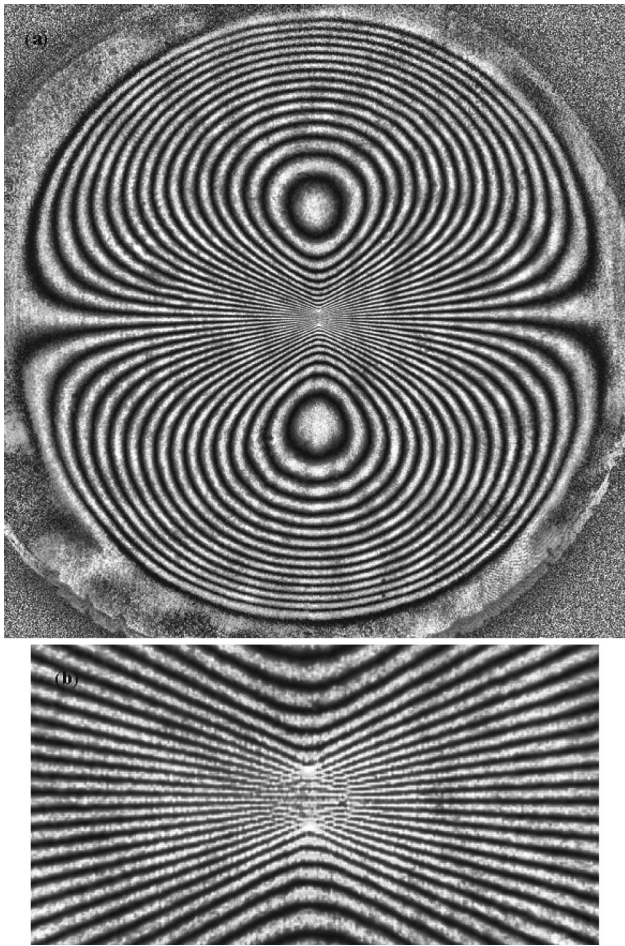
Fig. 5 Slope fringes obtained for a clamped silicon wafer subjected to central deflection: (a) Full view and (b) enlarged view near the center of the plate.
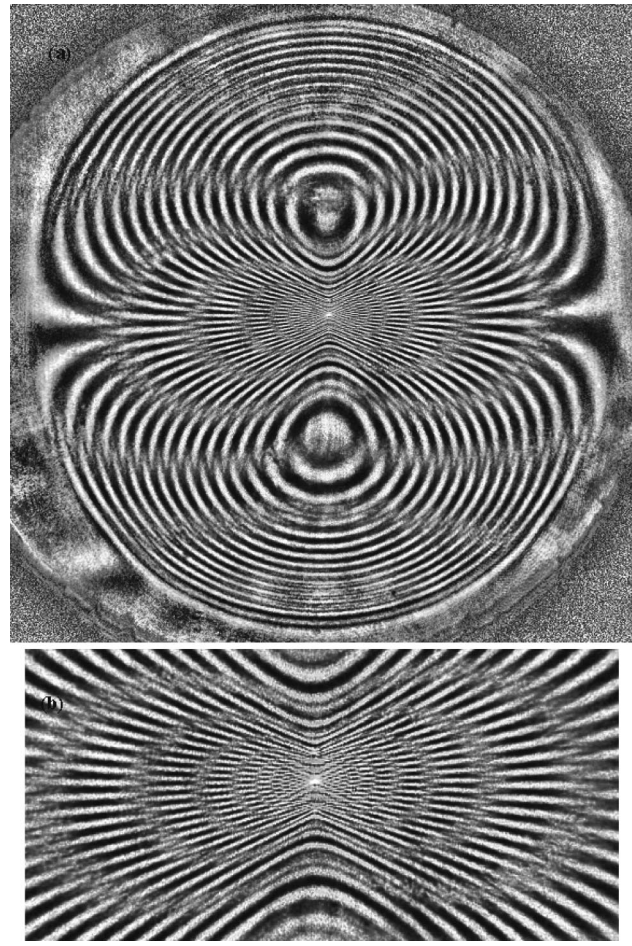

Fig. 6 Curvature fringes obtained for a clamped silicon wafer subjected to central deflection. (a) Full view and (b) enlarged view near the center of the plate.

the in-plane coordinates of the circular plate with a loading point as the origin. As discussed earlier, the fringe orders were assigned based on the boundary conditions of the problem, namely $\partial w/\partial y$ is zero along the x axis and $\partial^2 w/\partial y^2$ along the x axis at $(x = \pm a, y = 0)$. Figure 7 shows comparison between measured and predicted surface slopes along $(x = 0, y)$. Good agreement between the two is clearly evident. The slopes at the clamped edges are somewhat higher than the theoretical predictions, while they are lower at the peak value, possibly due to the fact that the theory assumes rigid clamp, while in reality epoxy glue essentially provides a certain degree of compliancy. The comparison between the measured curvature and the predictions is also very good along both the x and y axes of the plate, as shown in Figs. 8(a) and 8(b). The fringes as close as 0.5 mm from the center of the plate have been successfully extracted along the x axis, demonstrating the resolvability of dense fringes at this critical location.

6 Conclusions

The optical method of coherent gradient sensing which has been used widely in the dynamic fracture and failure mechanics community, is extended in this work to simulta-

neously measure slope and curvature fringes of thin structures in real time. Both slope and curvature fringe families occur at spatially distinct locations of the image plane. That is, highly discernable fringes representing slopes and curvatures can be obtained from the method without any additional postprocessing of the image plane recordings. Optical information is retrieved at spatial distances less than
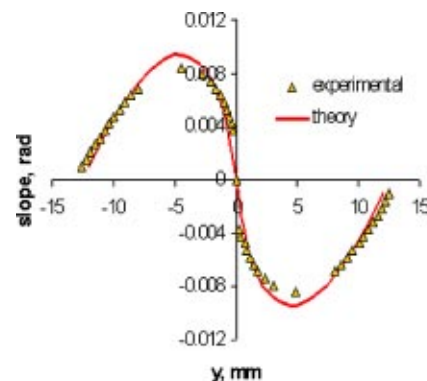

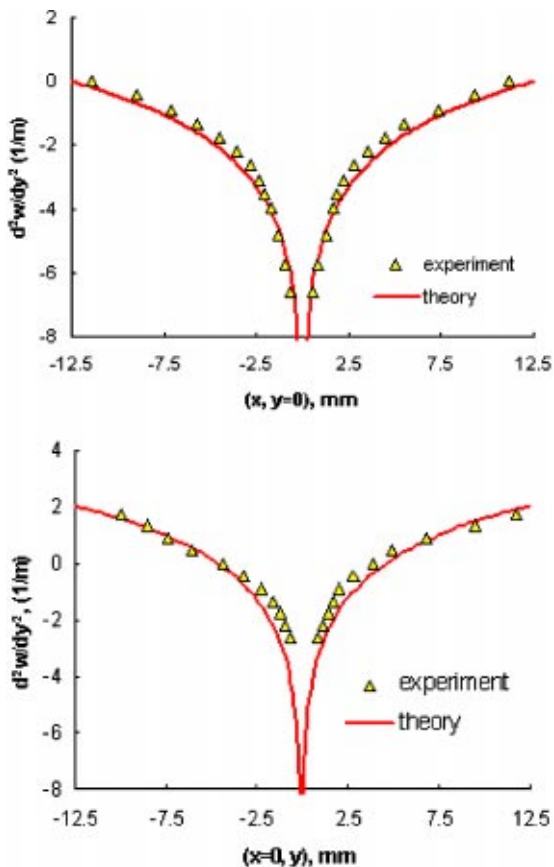**Fig. 7** Comparison between measured and predicted surface slopes.

Fig. 8 Comparison between measured and predicted curvature of silicon wafer along the *x* and *y* axes.

0.5 mm away from the loading point and compared successfully with the analytical solutions. Thus, numerical differentiation of optically measured slope data for determining curvature can be avoided. The measurements are demonstrated with a relatively high slope resolution of 2.64×10^{-4} radians/half-fringe and curvature resolution of 0.44 m^{-1} per half-fringe. These resolutions can be further enhanced, if necessary, by increasing the shearing distance between the gratings or by increasing the pitch of the Ronchi gratings.

Acknowledgments

References

1. L. B. Freund, "The mechanics of electronic materials," *Int. J. Solids Struct.* **37**, 185–196 (2000).
2. A. Assa, A. A. Betser, and J. Politch, "Recording slope and curvature contours of flexed plates using gratings shearing interferometer," *Appl. Opt.* **16**(9), 2504–2513 (1977).
3. T. Y. Kao and F. P. Chiang, "Family of grating techniques of slope and curvature measurements for static and dynamic flexure of plates," *Opt. Eng.* **21**, 721–742 (1982).
4. R. Ritter and R. Schettler-Koehler, "Curvature measurement by moiré effect," *Exp. Mech.* **23**, 165–170 (1983).
5. G. Subramanian and P. N. Akella, "A selective diffraction order based lens plane grating shearing interferometer for the study of bent plates," *J. Strain Anal.* **23**(2), 55–59 (1987).
6. G. Subramanian, K. Jancy Rose, and A. Subramanian, "A multiplexed grating shearing interferometer for reflection moiré analysis of partial slopes and curvatures of bent plates," *Experimental Techniques* **24**(5), 27–30 (2000).
7. K. Patorski, "Generation of the derivative of out-of-plane displacements using conjugate shear and moiré interferometry," *Appl. Opt.* **25**, 3146–3151 (1986).
8. U. Heise, "A moiré method for measuring plate curvature," *Exp. Mech.* **7**, 47–48 (1966).
9. F. P. Chiang and R. M. Juang, "Laser speckle interferometry for plate bending problems," *Appl. Opt.* **15**, 2199–2204 (1976).
10. Y. Y. Hung and A. J. Durelli, "Simultaneous measurement of three displacement derivatives using a multiple image-shearing interferometric camera," *J. Strain Anal.* **14**, 81–88 (1978).
11. H. V. Tippur, "Coherent gradient sensing: A Fourier optics analysis and applications to fracture," *Appl. Opt.* **31**, 4428–4439 (1992).
12. H. Lee, A. J. Rosakis, and L. B. Freund, "Full-field optical measurement of curvatures in ultra-thin-film-substrate systems in the range of geometrically nonlinear deformations," *J. Appl. Phys.* **89**, 6116–6129 (2001).
13. D. Post, B. Han, and P. If, *High Sensitivity Moiré*, Springer-Verlag, Berlin (1994).
14. K. Patorski, "The self-imaging phenomenon and its applications," in *Progress in Optics*, Vol. 27, E. Wolf, Ed., pp. 1–108, North-Holland, Amsterdam (1989).

Hareesh V. Tippur received his BS, MS, and PhD degrees from Bangalore University, Indian Institute of Science and the State University of New York–Stony Brook, respectively. He was a postdoctoral research fellow at California Institute of Technology before joining Auburn University in 1990, where he currently is an alumni professor of mechanical engineering. He has worked extensively in the areas of failure characterization and optical metrology. His work has resulted in moiré and speckle techniques for measuring three-dimensional displacement fields near cracks, rough-surface IR interferometry to study elastoplastic crack-tip deformations, and a new shearing interferometry called coherent gradient sensing for fracture mechanics studies. Optical metrology and failure mechanics of dissimilar material interfaces, functionally graded materials, and thin films/structures are among his current research interests. He has received several recognitions from professional societies including being elected a fellow of the American Society of Mechanical Engineers and receiving the Hetenyi award from the Society for Experimental Mechanics and the Outstanding New Mechanics Educator award from the American Society for Engineering Education.